Characterizing the Central Structure of a Mesoscale Eddy-Ring Dipole in the Mozambique Channel from In-Situ Observations

Pierrick Penven[1], Jean-Francois Ternon[2], Margaux Noyon[3], Steven Herbette[1], Gildas Cambon[1], Caroline Comby[4], Pierre L'Hégaret[1], Bernardino S. Malauene[3,5], Claire Ménesguen[1], Fialho Nehama[6], Gustav Rauntenbach[7], Yula Rufino[6], Floriane Sudre[4]

[1]Univ. Brest, CNRS, Ifremer, IRD, Laboratoire d'Océanographie Physique et Spatiale (LOPS), IUEM, Plouzané, France
[2]Univ. Montpellier, CNRS, Ifremer, IRD, Marine Biodiversity exploitation et conservation (MARBEC), Sète, France
[3]Institute for Coastal and Marine Research (CMR), Nelson Mandela University, Gqeberha, South Africa
[4]Aix Marseille Univ, Univ Toulon, CNRS, IRD, Mediterranean Institute of Oceanography (MIO), Marseille, France
[5]Instituto Oceanográfico de Moçambique (InOM), Maputo, Mozambique
[6]Escola Superior de Ciencias Marinhas e Costeiras (ESCMC), Quelimane, Mozambique
[7]South African Environmental Observation Network, Egagasini Node, Cape Town, South Africa

Key Points:

- First high-resolution in-situ observations into a mesoscale dipole formed by a ring and a cyclonic eddy in the Mozambique Channel
- The dipole central jet swiftly transports shelf properties offshore, causing patchiness and layering in the cyclonic eddy
- Vertical velocities from the omega equation reveal the impacts of the dipole and of a smaller meander in the front

Corresponding author: Pierrick Penven, `pierrick.penven@ird.fr`

Abstract

During the RESILIENCE cruise aboard the R/V Marion Dufresne II (April 19-May 24, 2022), a high-resolution in-situ observation campaign investigated a mesoscale dipole in the Mozambique Channel, composed of a large anticyclonic ring and a cyclonic eddy. Using an innovative adaptive sampling strategy to track its movement, we employed continuous observing systems, including a Moving Vessel Profiler and Acoustic Doppler Current Profilers, to capture high-resolution vertical sections. The results revealed a distinct dipolar structure: The 250 km-wide anticyclonic ring featured low chlorophyll and homogeneous waters, while the smaller cyclonic eddy exhibited higher chlorophyll concentrations and pronounced salinity variations. These include patches, vertically stacked layers, and filaments, reflecting a mix of contrasted water masses from the southern Mozambique Channel and the Sofala Bank. A central jet between the eddies exhibited horizontal velocities up to 130 cm s^{-1}, facilitating significant offshore transport exceeding 10 Sverdrups in the upper 250 m and emphasizing the dipole's role in eastward water movement. Vertical velocities, derived from the Quasi-Geostrophic Omega equation, highlighted the influence of smaller-scale structures in driving vertical motions, reaching 40 m day^{-1} at depth. Lagrangian particle trajectories revealed the dipole's spiraling structure and its connectivity to coastal waters. These findings show that Mozambique Eddy-Ring Dipoles efficiently transport properties from the continental shelf to the open ocean, enhancing regional ecosystem connectivity. This work provides new insights into their biogeochemical, biological and ecological significance, challenging traditional cyclonic/anticyclonic eddy paradigms, and setting the foundation for future studies on mesoscale dipoles in the region.

Plain Language Summary

During the RESILIENCE cruise aboard the R/V Marion Dufresne II from April 19 to May 24, 2022, we conducted detailed observations in the Mozambique Channel to study a specific ocean feature called a mesoscale dipole. It consists of two large swirling oceanic structures: an anticyclonic ring and a cyclonic eddy, with a strong current flowing to the southeast between them. Using continuous observing techniques from towed instruments, we measured ocean properties and how water moved within this dipole. We found that the anticyclonic ring extends over 250 km and had low levels of chlorophyll and uniform waters. In contrast, the cyclonic eddy, which is smaller, had higher chlorophyll levels and more varied salinity. The central current between these two features moved at speeds up to 130 cm s^{-1} and is responsible for significant water transport away from the Mozambican coast. We revealed that smaller structures, rather than the dipole itself, drove most vertical water movements. The cyclonic eddy showed complex salinity patterns due to the presence of different water masses spiralling around each other. These findings help us understand how such ocean features affect water movement and will guide future research into their impact on the marine environment.

1 Introduction

Located in the southwest Indian Ocean, between Madagascar and the African continent, the Mozambique Channel experiences an average southward oceanic transport of approximately 14 Sv (1 Sv = 10^6 m^3 s^{-1}) (Ganachaud & Wunsch, 2000), with estimates ranging from 5 to 18 Sv (Harlander et al., 2009) and with a large standard deviation of $\sim$ 15 Sv (Ullgren et al., 2012). This region is indeed among the most turbulent in the world's oceans, with surface eddy kinetic energy exceeding 1500 cm^2 s^{-2} (Penven et al., 2014). The circulation is dominated by large anticyclonic rings, whose generation is linked to variations in the transport of the South Equatorial Current (Backeberg & Reason, 2010). These Mozambique Channel Rings are distinct from more common geostrophic eddies due to their greater size (with radii exceeding 100 km) and typical vorticity structure (Halo et al., 2014). They can reach diameters of up to 350 km and extend vertically to depths of 2000 m, with sub-surface currents often exceeding 1 m s^{-1} (de Ruijter et al., 2002; Schouten et al., 2003; Halo et al., 2014). Cyclonic eddies are also present, generally smaller in diameter (Halo et al., 2014; Saëtre & da Silva, 1984; Schouten et al., 2003). Anticyclonic and cyclonic eddies may occasionally pair, generating a dipole (Tew-Kai et al., 2009; Roberts et al., 2014).

In the Mozambique Channel, rings and eddies shape marine ecosystems at all trophic levels, from phytoplankton to top predators (Barlow et al., 2014; Lamont et al., 2014; Jaquemet et al., 2014; Tew-Kai et al., 2009; Weimerskirch et al., 2004). The multidisciplinary observation program MESOBIO (2008-2010) focused on quantifying the role of eddies in the abundance and spatial distribution of living organisms from phytoplankton up to top predators in the Mozambique Channel (Ternon, Bach, et al., 2014). This program highlighted the dominant effects of eddy-topography and eddy-eddy interactions on marine biological production in the region (José et al., 2014; Roberts et al., 2014). Mozambique Channel rings and eddies also influence environmental conditions on the continental shelf by promoting the upwelling of nutrient-rich deep waters (Lamont et al., 2010; Malauene et al., 2014, 2018). Coastal waters, likely loaded with nutrients and plankton, can be transported seaward at the edges of eddies, potentially forming filaments (Figure 1) (Roberts et al., 2014). A modeling study identified eddy exchange between the coast and the open sea as the predominant factor for primary productivity in the central Mozambique Channel (José et al., 2016). The implications are significant for fisheries management and the conservation of threatened species. For example, Malauene et al. (2024) have recently demonstrated from a model that offshore eddy transport could cause significant loss of shrimp larvae from Sofala Bank, the large shelf along the Mozambique coast (Figure 1).

As a compelling example of such offshore transport, Roberts et al. (2014) highlighted the potential efficiency of a dipole, comprising an anticyclonic Mozambique Channel ring and a cyclonic eddy, in driving upwelling and transporting material from the shelf to offshore regions, effectively fertilizing the oligotrophic waters of the channel. In 2007, Ternon, Roberts, et al. (2014) did a Ship mounted Acoustic Doppler Current Profiler (SADCP) transect across a dipole offshore of Sofala Bank in the central Mozambique Channel. They measured subsurface velocities reaching 130 cm s^{-1} between the eddies. Ni et al. (2020) have shown that mesoscale eddy dipoles are actually abundant in the world's oceans, particularly in the Mozambique Channel (see their Figure 3), and can generate significant vertical velocities through frontogenesis and frontolysis. In the central Mozambique Channel, between 17°S and 20°S, mesoscale dipoles appear to occur about three times a year (Huang et al., 2024). However, despite their striking appearance on ocean color images (Figure 1), the in-situ structure, dynamics, and ecological implications of Mozambique Channel mesoscale eddy-ring dipoles remain poorly understood. While it is known that these large dipoles do exist, their fine-scale in-situ structure and their implications for marine biology remain largely unexplored. It is hypothesized that these dipoles may favor biological production by promoting upwelling and transporting coastal ocean properties offshore.

The first leg of the RESILIENCE (fRonts, EddieS, and marIne LIfe in the wEstern iNdian oCEan) multidisciplinary oceanographic cruise aboard the R/V Marion Dufresne II in April 2022 focused on investigating the central structure of such an eddy-ring dipole. The primary objectives were to characterize the structure at the center of the dipole, understand its origins and evolution, and assess its potential implications for transport, biogeochemical cycles, and ecological processes in the Mozambique Channel. Given that previous observational studies in the region were often constrained by horizontal resolution, typically classifying features as cyclonic eddies, anticyclonic eddies, or the intervening region when assessing eddy influence on marine ecosystems (Ternon, Bach, et al., 2014; Barlow et al., 2014; Lamont et al., 2014; Jaquemet et al., 2014), this article aims to provide a more detailed description of the primary physical processes underpinning the biogeochemical, biological, and ecological studies conducted during the first leg of the RESILIENCE cruise.

Following a presentation of the sampling strategy and measurement methods, in-situ and satellite observations are shown to characterize the dipole and track its origin, evolution, and decay. In-situ data are then integrated to delineate the main central structure of the dipole and to assess vertical velocities induced by its presence. A Lagrangian analysis is utilized to trace the origin of water masses within the dipole and estimate the time elapsed since their departure from the shelves. These analyses underscore the significant roles of stirring and horizontal transport in influencing the oceanic properties associated with dipoles in the Mozambique Channel.

2 Material and methods

2.1 General cruise presentation

The RESILIENCE cruise was a multidisciplinary oceanographic expedition which investigated the intricate relationships between oceanic fine-scale processes and marine life, spanning from phytoplankton, zooplankton and micronekton to large marine mammals and seabirds. The expedition focused on the turbulent regimes of western boundary currents between the Mozambique Channel and the Agulhas Current (Ternon et al., 2022, 2023). Conducted aboard the R/V Marion Dufresne II from April 19 to May 24, 2022, the cruise embarked and concluded at La Réunion Island. In this work, we focus on the first leg of the expedition, which was conducted from April 25 to May 1, 2022, and was centered in the central Mozambique Channel, approximately 60 nautical miles northwest of Bassas da India (Figure 1).

2.2 Sampling strategy

The sampling strategy was adaptive, guided by real-time thermosalinograph data and satellite observations to optimize the cruise track. The rapid southeastward movement of the dipole allowed for extensive sampling of its central structure. The cruise track comprised a series of high-resolution cross-dipole sections, each lasting approximately 5 hours at a steaming speed of 5 knots. These sections were interspersed with 1000-meter-deep stations according to the following scheme: a station in the cyclonic (anticyclonic) eddy, a 5-hour sampling section, a station near the central front, another 5-hour sampling section, and finally a station in the anticyclonic (cyclonic) eddy. The original plan followed a regular zig-zag shape but was adjusted in real-time to adapt to the southeastward propagation of the dipole towards the center of the Channel.

The resulting cruise track consisted of 13 high resolution vertical sections (only 9 with in-situ temperature-salinity measurements) and 13 stations (all at 1000 meters), as depicted on Figure (1). Although the latitude-longitude track appeared disorganized, eddy ring interactions led to a rapid southeastward movement of the dipole. This allowed sampling in the center and the difluent region of the hyperbolic circulation associated with the dipole (as explained in section 3.3.1).

2.3 In-situ observations

High-resolution in-situ sampling was conducted using a Moving Vessel Profiler (MVP 200), an undulating device towed at the rear of the ship at about 5 knots. The MVP, equipped with an SBE CTD911+ probe (measuring pressure, conductivity and temperature at 24 Hz) and an ECO FLNTU probe (measuring fluorescence and turbidity at 1 Hz), profiled the water column from the surface to 300 meters depth. It made vertical

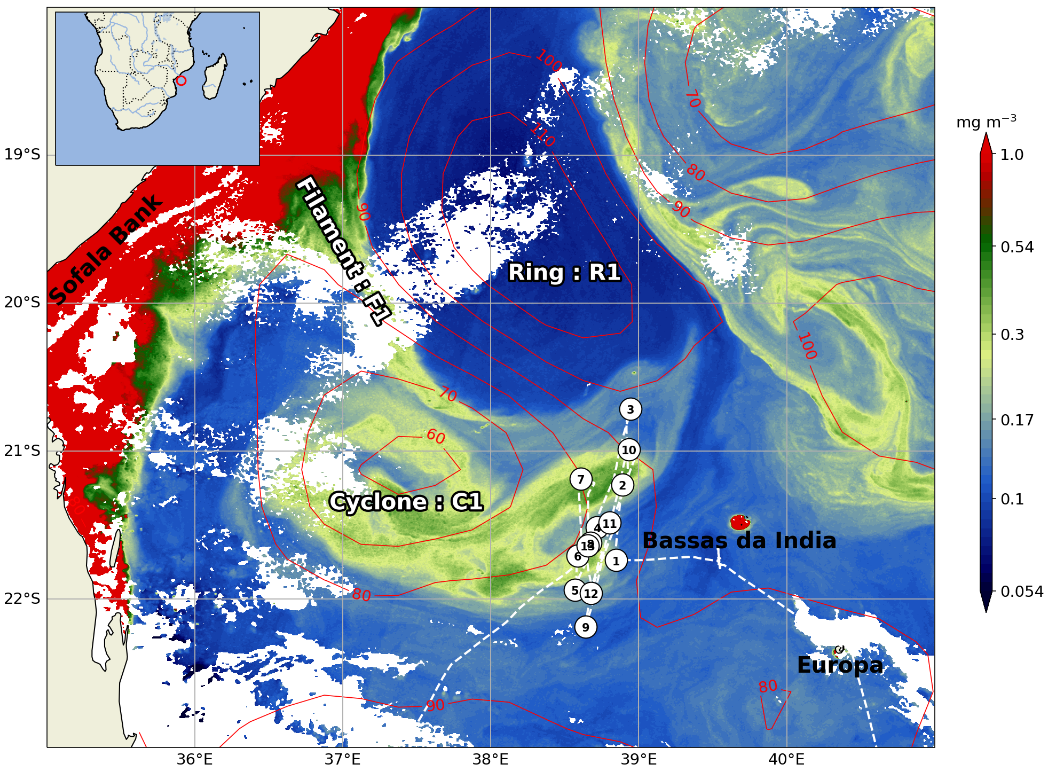

Figure 1. Dipolar structure formed by a Mozambique Channel ring (R1) and a cyclonic eddy (C1) in the central Mozambique Channel. Chlorophyll concentration [mg m^{-3}] and SSH (1 red contour / 10 cm) for April 16, 2022, about 10 days after dipole formation. The scientific cruise track (from April 19 to May 24, 2024) is represented as a white dashed line and station numbers are given into white circles. A filament (F1) of enhanced chlorophyll and coastal waters is swiped offshore by the interactions of R1 with Sofala Bank. Another filament has been captured previously by C1 and spirals into the eddy core.

profiles approximately every 1.5 km by free falling and being winched back up in a parabolic path. MVP operations were not conducted on sections 5, 8, and 9.

MVP temperature and salinity measurements have been post-processed using the method described by L'Hégaret et al. (2023). First, temperature and conductivity offsets have been adjusted using nearby CTD stations, with constant values of 0.2°C and 0.1 mS cm^{-1}, respectively. Misalignments between temperature and conductivity measurements, which affects salinity values, were corrected by applying a lag to temperature based on the device's vertical velocity. Optimal correction coefficients were determined by minimizing salinity dispersion. Thermal mass error, causing discrepancies between ascending and descending profiles, has been corrected by using ascending profiles as references and minimizing the area between successive temperature-salinity curves. Uncertainty for each parameter has been quantified by comparing corrected MVP measurements with nearby CTD stations, resulting in uncertainties of 0.05°C for temperature and 0.01 g kg^{-1} for salinity. Data were box-averaged using the median on a regular vertical grid with 1-meter resolution and were linearly interpolated horizontally using time as interpolant (1 min resolution). A 5 points running mean has been applied to filter possible remaining noise. The final datasets and documentation are available on the open scientific data repository in marine sciences SEANOE (SEA scieNtific Open data Edition) (L'Hégaret et al., 2024).

In between MVP transects, 13 CTD casts were conducted using a rosette frame equipped with an SBE 911+ CTD and carrying up to 20 Niskin bottles, each with a capacity of 12 liters, deployed to a depth of 1000 meters. The CTD was equipped with sensors for pressure, temperature, conductivity (two sensors), oxygen (two sensors), PAR, fluorometer, transmissometer, S-PAR, and altimeter. These sensors were calibrated at the Sea-Bird Scientific factory in early 2021 and checked at LOPS-IFREMER in October 2021. Post-cruise calibration of the CTD data has been performed at LOPS-IFREMER (Le Bihan, 2024).

Horizontal currents were measured using one-minute interval continuous observations from a 150 kHz hull-mounted RDI Ocean Surveyor Acoustic Doppler Current Profiler (ADCP). This instrument estimates water velocities through the Doppler effect using four beams. It operates over a depth range of 0–250 m, comparable to the MVP's range, with an 8 m vertical resolution. The collected data were processed and analyzed using CASCADE software v7.2 (Kermabon et al., 2018).

Sea surface temperature (SST) and salinity (SSS) were continuously monitored using an SBE45 thermosalinograph (TSG). Regular verification through sampling and conductivity measurements ensured the accuracy of salinity data. TSG data are calibrated against these controls data points using the TSG-QC software developed by the IRD-IMAGO laboratory in Brest. Quality control measures yielded an uncertainty of approximately 0.005°C for SST and 0.02 g kg^{-1} for SSS.

2.4 Satellite images and dipole tracking

Surface Chlorophyll-a maps were generated from near real-time multi-sensor data, specifically from Sentinel-A and Sentinel-B, with a resolution of 300 m. These data are distributed by Copernicus Marine Services based on global ocean satellite observations (Colella et al., 2024).

Given the large size of rings and eddies in the Mozambique Channel, their signals are well captured in satellite altimetry (Halo et al., 2014). Hence, sea surface height (SSH) data from daily absolute dynamic topography, gridded at 1/4°, was used to monitor their evolution over time. These data are distributed by Copernicus Marine Services (Pujol, 2024).

The anticyclonic ring (R1) and the cyclonic eddy (C1) pair, forming the dipole in Figure (1) was detected using a method based on SSH closed contours and the Okubo-Weiss parameter (Halo et al., 2014). The dipole center was defined as the middle between the boundaries of R1 and C1 along the line connecting R1 and C1 centers. The dipole axis was established by drawing a line perpendicular to the line connecting the centers of R1 and C1, passing through the dipole center. A moving orthogonal frame was then defined using the dipole center and axis (as the X-axis) to represent the variables and sections relative to the dipole structure.

2.5 Interpolations and mapping

We employed the objective analysis method described by Arhan and De Verdière (1985) to map scalars and 2D vector fields within the dipole frame on a regular grid with a resolution of 2.5 km. As demonstrated by Arhan and De Verdière (1985) and Pivan et al. (2015), this method is well-suited for describing mesoscale oceanic structures. Considering the sizes of eddies in the Mozambique Channel (Halo et al., 2014), we used a decorrelation length scale of 100 km.

2.6 Vertical velocities

Eddying structures are frequently associated with marine biological production due to their vertical velocities (McGillicuddy & Robinson, 1997; Oschlies & Garçon, 1998). The Omega equation has been used in the past to derive the vertical velocities in mesoscale eddies (Buongiorno Nardelli, 2013; Rousselet et al., 2019) and dipolar structures (Legal et al., 2007; Pidcock et al., 2013; Ni et al., 2020). In this study, we utilized ADCP horizontal currents and MVP temperature and salinity data, all gridded on a regular grid with 2.5 km horizontal and 8 m vertical resolution, to derive a vertical velocity w from the QG Omega equation (Hoskins et al., 1978; Pollard & Regier, 1992; Pinot et al., 1996; Legal et al., 2007; Pidcock et al., 2013; Rousselet et al., 2019; Ni et al., 2020):

$$N^2 \nabla_h^2 w + f^2 \frac{\partial^2 w}{\partial z^2} = 2\nabla.\mathbf{Q} \tag{1}$$

Where $N(z)$ is the mean Brunt-Väisälä frequency, f the Coriolis parameter, $\nabla_h^2 = \frac{\partial^2}{\partial x^2} + \frac{\partial^2}{\partial y^2}$, and the $\mathbf{Q}$-vector is defined as:

$$\mathbf{Q} = \frac{g}{\rho_0}\left(\frac{\partial u}{\partial x}\frac{\partial \rho}{\partial x} + \frac{\partial v}{\partial x}\frac{\partial \rho}{\partial y}, \frac{\partial u}{\partial y}\frac{\partial \rho}{\partial x} + \frac{\partial v}{\partial y}\frac{\partial \rho}{\partial y},\right) \tag{2}$$

Here, g represents gravitational acceleration, ρ_0 is the mean density, u and v are the horizontal components of velocity field, which is here non-divergent for each vertical level since it is obtained from a 2D vectorial objective analysis (Arhan & De Verdière, 1985) of ADCP measurements, and ρ denotes the density anomaly. We used 2^{nd} order centered schemes on the horizontal and the vertical for equation 1. $\nabla.\mathbf{Q}$ was computed with 4th order centered schemes. The inversion was done using a Jacobi iterative method, with Dirichlet conditions (w = 0) for lateral and vertical (z = 0 and z = -250 m) boundaries. A test using Neumann (non-gradient) boundary conditions at z = -250 m produced similar results at intermediate depths. Applying Neumann conditions laterally increased vertical velocities across the domain, though the central pattern remained present. Tests with varying horizontal grid resolutions (dx = 10, 5, and 2.5 km) revealed weak sensitivity and demonstrated satisfactory convergence of the solution with increasing resolution. Variations in gridding decorrelation scales for the objective analysis affected the absolute values of vertical velocities, but the overall pattern remained consistent.

2.7 Lagrangian backtracking

To trace the origin of surface water masses within the dipole, we introduced Lagrangian virtual particles into the structure. These particles were advected backward in time using geostrophic currents derived from daily AVISO absolute dynamic topography. Velocities were interpolated linearly in both space and time. Particle transport was performed using a second-order Adams-Bashforth-Moulton predictor-corrector scheme with a 2-hour time step. Tests have demonstrated that this scheme provides adequate stability and precision for the scales addressed in this study.

3 Results

3.1 A Mozambique Channel mesoscale eddy-ring Dipole

April 16, 2022, was the last clear day before arrival of our vessel in the area (Figure 1). A chlorophyll image at 300 m resolution, captured by the Sentinel 3A and 3B satellites, along with altimetry sea surface height contours, had provided a synoptic view of the area of interest: a fully formed dipole consisting of a Mozambique Channel anticyclonic ring (R1) to the north and a mesoscale cyclonic eddy (C1) along its southern flank. This image was taken approximately 10 days after the dipole formation.

The fully developed anticyclonic ring R1, centered at 19.5°S, 38°E, is characteristic of the Mozambique Channel (de Ruijter et al., 2002; Halo et al., 2014; Penven et al., 2014). It extended over 250 km and trapped waters with low surface chlorophyll concentrations. Typical of Mozambique Channel rings, it followed the shelf edge while propagating southward (Halo et al., 2014).

Surface chlorophyll concentration (and likely dissolved organic matter) is higher (greater than 1 mg m^{-3}) on the Sofala Bank, a large, shallow shelf extending along the Mozambican coast from the Bazaruto Archipelago around 22°S to near Angoche around 16°S. From there, a chlorophyll filament (F1 in Figure 1) was stirred around the edge of the ring, marking R1's southern boundary. This pattern is typical for the Mozambique Channel (José et al., 2014; Roberts et al., 2014).

Extending over approximately 100 km, the cyclonic eddy C1, centered at 21°S, 37.5°E, was smaller than R1, consistent with the region's Rossby radius of deformation, which is about 50 km (Chelton et al., 1998; Halo et al., 2014). Higher surface chlorophyll concentrations of around 0.3 mg m^{-3} were found in C1's core (Figure 1). The high-resolution satellite images revealed that the chlorophyll pattern in C1 formed a spiral. Chlorophyll images from early April (not shown) indicated that this structure was a remnant of a previous filament generated on April 1, 2022, in a similar manner to F1, by the interaction of R1 with the Sofala Bank. This structure became trapped as C1 approached R1 and spiraled into the eddy core (Figure 1).

By April 16, 2022, R1 and C1 were clearly interacting, forming a dipole. Filament F1, which delineated the southern edge of R1, followed the dipole's central jet. This central section of the dipole exhibits contrasting surface chlorophyll patterns and constitutes the focal point of the RESILIENCE scientific campaign.

3.2 Dipole formation and evolution

3.2.1 Origins of R1 and C1

Due to their large horizontal extensions and significant SSH amplitudes (nearly 40 cm for R1 and 25 cm for C1; see Figure 1), R1 and C1 were easily detectable by gridded altimetry products. An eddy tracking method, utilizing a combination of the Okubo-

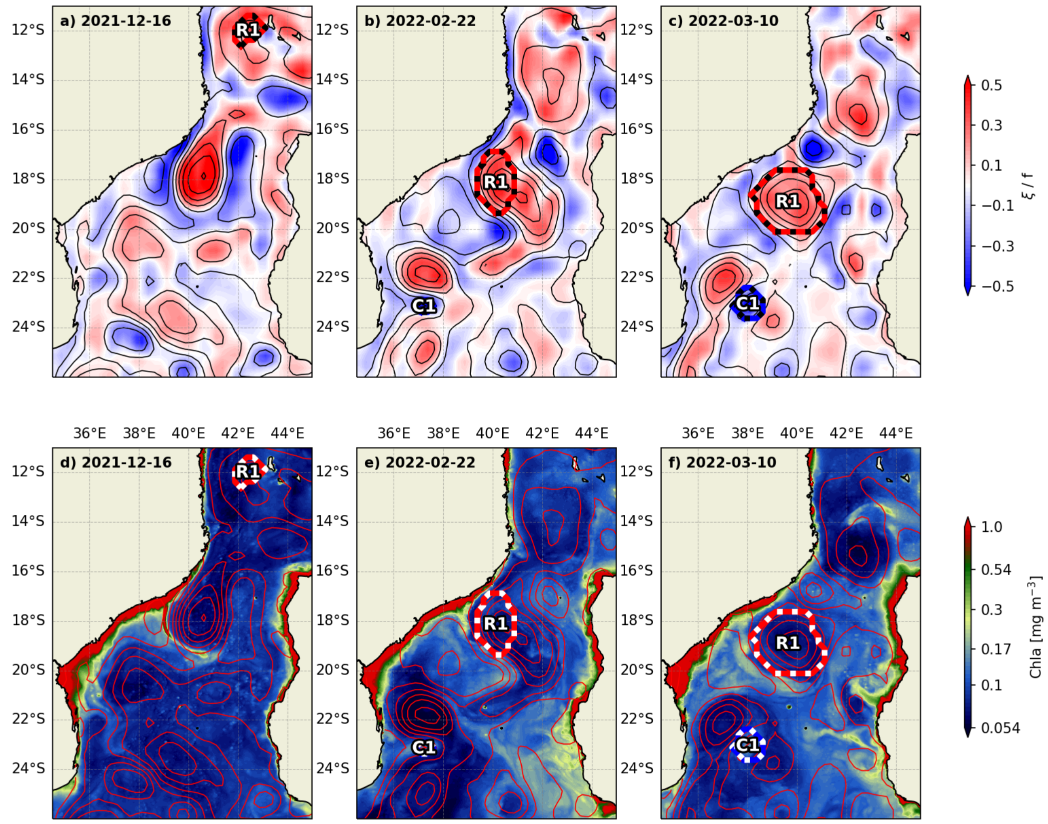

Figure 2. Origins of the dipole. Top panels: relative vorticity divided by the Coriolis parameter (colors) and SSH (1 black contour / 10 cm). Bottom panels: chlorophyll concentration [mg m^{-3}] and SSH (1 red contour / 10 cm) for December 16, 2021 (left), February 22, 2022 (middle) and March 10, 2022 (right). The eddy contours are visible as dashed lines (red for R1, blue for C1).

Weiss parameter and SSH closed contours (Halo et al., 2014), was employed to monitor R1 and C1 over time, from their generation to their dissipation.

Figure (2) shows the origins of R1 and C1 before they merged to form a dipole. R1 was first observed in the Northern Mozambique Channel, west of the Comoros Archipelago, around mid-December 2021 (Figure 2-a,d). It grew while propagating southward along the western side of the channel (Figure 2-b,c,e,f). By March 10, 2022, R1 was fully developed, reaching an eddy diameter of nearly 300 km. A filament of enhanced chlorophyll concentration was already noticeable along its southern flank (Figure 2-d,e,f).

C1 was generated around February 22, 2022 (Figure 2-b), through the extraction of cyclonic vorticity from the shelf by another anticyclonic ring in the Southern Mozambique Channel, forming an Inhambane cyclone (Cossa et al., 2016). C1 was associated with enhanced chlorophyll, probably also originating from the shore (Figure 2-e). After its generation, C1 was advected around the southern side of the ring and formed a tripolar structure (two anticyclones surrounding a cyclone) by March 10, 2022 (Figure 2-e).

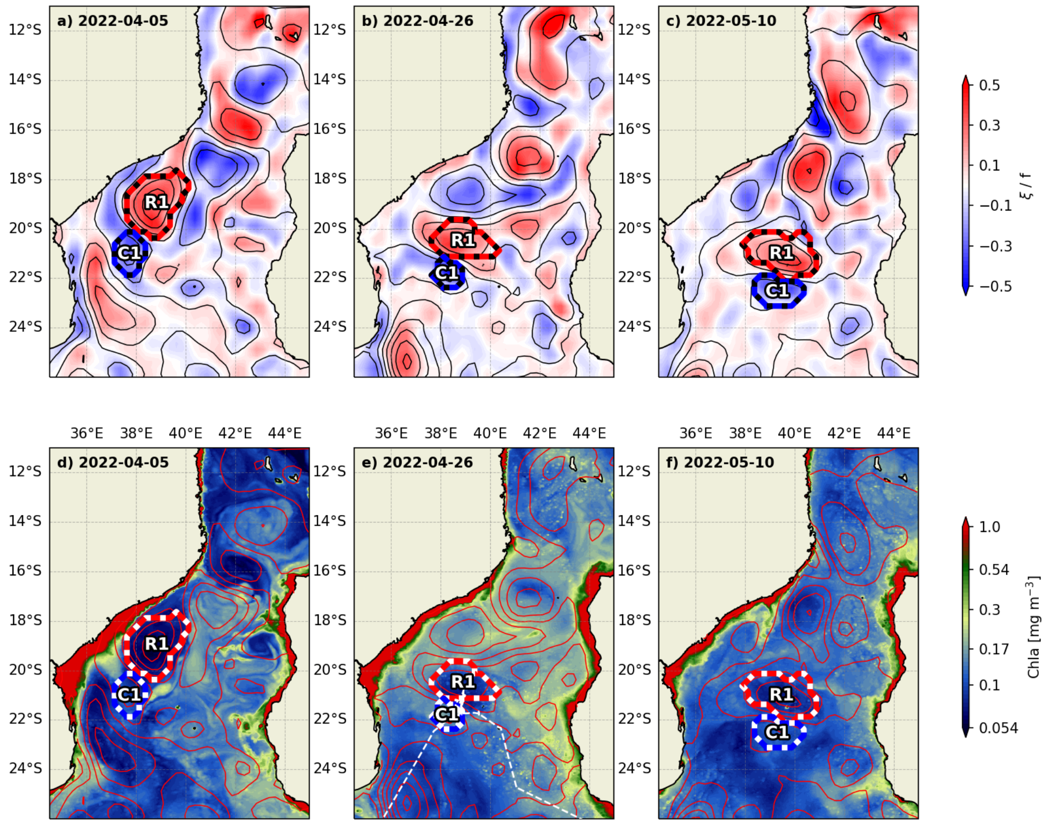

Figure 3. Following the dipole. Same as Figure (2) for April 5 (left), April 26 (middle) and May 10 (right), 2022. The white dashed line on panel e) represents the cruise track which took place from April 25 to May 1, 2022. The dipole is fully formed and propagates by self advection toward the middle of the Channel.

3.2.2 Following the dipole

In March 2022, while R1 slowly propagated southward along the western side of the Mozambique Channel, as a classic Mozambique Channel Ring (Halo et al., 2014), the anticyclonic ring centered at 22°S, 36.5°E (Figure 2-c) advected C1 northward. By the end of March 2022, C1 had moved close to R1's vicinity (Figures 2-c and 3-a). In April 2022, they formed a dipole that began to propagate southeastward toward the center of the Mozambique Channel (Figure 3).

Figure (4-a) illustrates the radii of R1 and C1 as determined by the eddy tracking algorithm, along with the distance between their centers. According to Ni et al. (2020), a dipole forms when the combined radii of the eddies at least equal the distance between their centers. This condition was met from April 20 to May 14, 2022, marking a lifespan of 24 days, nearly three times longer than the global average lifespan of 8.5 days reported by Ni et al. (2020). During this period, the dipole traveled southeastward, covering a total distance of 240 km, intersecting with the cruise tracks shown on Figure 3. Moreover, Figure (4-b,c,d) shows that the dipole traveled at an almost constant speed of 8.8 km day^{-1} with a mean bearing of 115° over the duration of the leg, from April 25 to May 2, 2022.

After May 10, the dipole began interacting with the topographical features associated with Bassas da India, causing it to stop propagating southeastward (Figure 4-b,c).

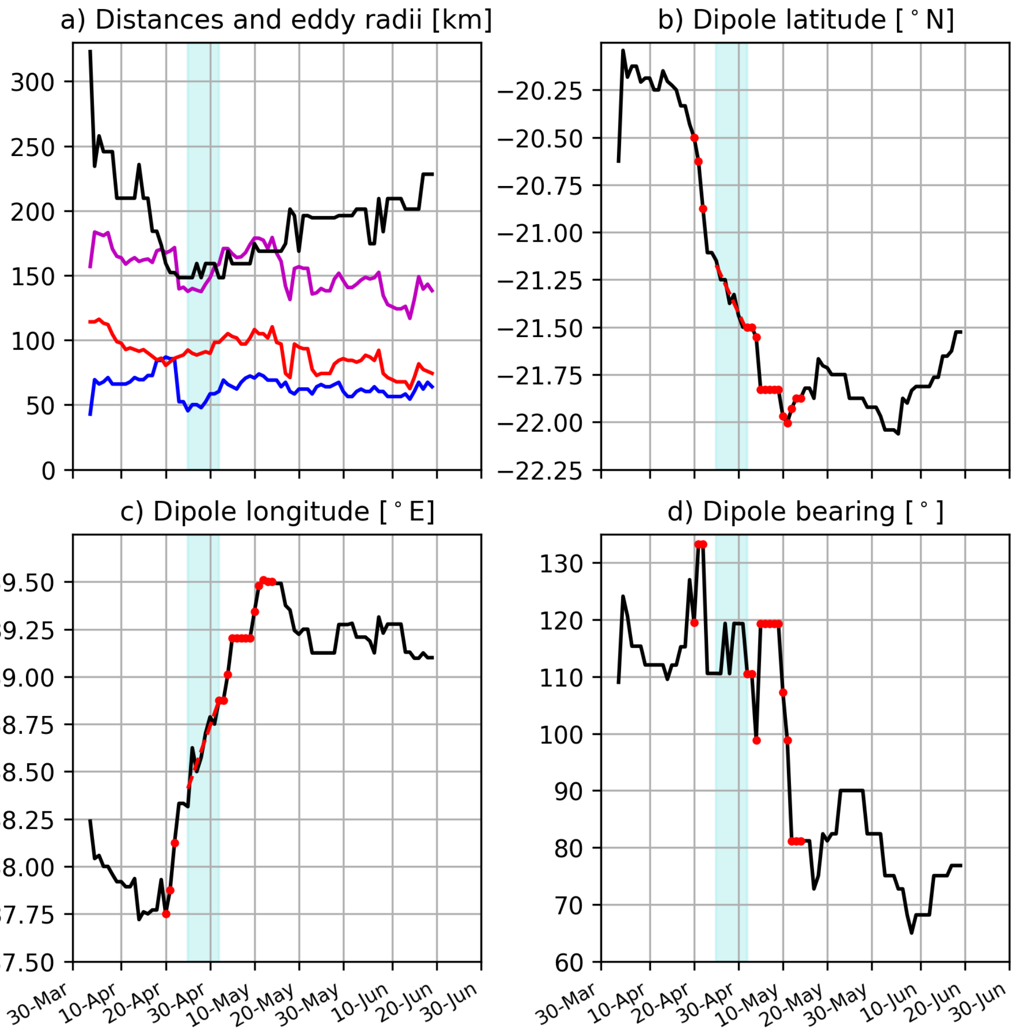

Figure 4. Dipole tracking. a) Eddy radii (R1: red; C1: blue; R1+C1: purple) and distances between eddy centers (black) from April to June 2022. b) Dipole center latitudes [°N]. c) Dipole center longitudes [°E]. d) Dipole bearing [°]. R1 and C1 are approaching each other in the beginning of April to reach a full dipole interaction (distance between centers < R1+C1; red dots) the 20/4/2022. The light blue region on each panel mark the duration of Leg 1. The red dashed line represents a continuous displacement at a constant speed of 8.8 km day^{-1} in the E-SE direction (115°) over the duration of Leg 1.

The dipole axis rotated counter-clockwise toward the northeast (Figure 4-d), while R1 and C1 started to drift apart (Figure 4-a). By the end of June, the dipole had lost its coherence. C1 dissipated rapidly afterward, while a smaller R1 continued its journey southward.

3.3 Horizontal characteristics of the dipole

3.3.1 Tracking the dipole and horizontal mapping

We leveraged the dipole's continuous movement during Leg 1 to remap the observations in a moving frame that followed the structure. Examining the longitude and latitude time series in Figure 4b-c reveals that the dipole traveled along an almost straight path at a constant speed during the cruise period (April 25 to May 2, 2022). This motion is highlighted by the red dashed lines in Figures 4b and 4c. From this displacement, we calculated a constant speed of 8.8 km day^{-1} in the E-SE direction (115°). This information was used to adjust the frame over time, thereby preventing the introduction of spurious deformations when interpolating data onto the grid. Figure 5 depicts a remapping of altimetry SSH and altimetry-derived geostrophic velocity vectors for each day during Leg 1. Underway SADCP velocities at 48 m depth are represented in the moving frame as red arrows for each day, along with station numbers. A depth of 48 meters is chosen here and throughout the manuscript to be below the Ekman layer, allowing direct comparison with the subsurface geostrophic flow. The frame displacement has been subtracted from the horizontal velocity vectors.

In the dipole center, velocities could exceed 130 cm s^{-1}. The SADCP 48 m velocities generally matched the altimetry-derived velocities, confirming the effectiveness of gridded satellite altimetry products in representing large mesoscale structures such as R1 (Ternon, Roberts, et al., 2014). However, this correlation was less accurate between station 1 and station 2 (Figure 5-a), and towards the end of Leg 1, when we passed the center of C1 after station 13 (Figure 5-f). Throughout the 6 days of Leg 1, the dipole appeared well-centered and quasi-stationary relative to the moving frame (Figure 5). The cruise track indicates that we have mostly sampled the eastern difluent side and the core of the dipole.

We then employed a scalar and vectorial objective analysis with a decorrelation scale of 100 km (Arhan & De Verdière, 1985) to represent TSG SSS and 48 m SADCP velocities on a single regular grid with a 2.5 km resolution, centered on the dipole (Figure 6, which includes station and section locations). As shown in Figure 6, there is a good correspondence between gridded SADCP and altimetry-derived velocities, validating the mapping procedure at the mesoscale. The differences in SSS between R1 and C1 are notable in Figure 6. R1 exhibits higher ($\sim$ 35.3 g kg^{-1}) and homogeneous SSS, while C1 displays lower ($\sim$ 34.9 g kg^{-1}) and more patchy SSS.

3.3.2 Horizontal velocities and transport

The vectorial objective analysis was applied to SADCP velocities to obtain a stream function for each vertical layer on the regular horizontal grid. The resulting subsurface currents (at 48 m, to be below the surface layer) reveal a mean central jet approximately 50 km wide, with velocities reaching 130 cm s^{-1} around 10 km from the dipole center (Figure 7-a). Dynamic height anomalies computed from the SADCP streamfunction at 48 m ($\eta = \frac{f}{g}\psi_{48}$, where η is the dynamic height, f the Coriolis parameter, g the gravity acceleration and ψ_{48} the SADCP streamfunction at 48 m, below the Ekman layer) are comparable to altimetry SSH anomalies (Figure 7-b).

We averaged horizontal velocities ($\bar{u}$ along the dipole ; $\bar{v}$ across the dipole) down to 250 m where there are sufficient high-quality 150 kHz SADCP observations. This provided an integrated image of the upper ocean structure (Figure 7-d). Close to the dipole

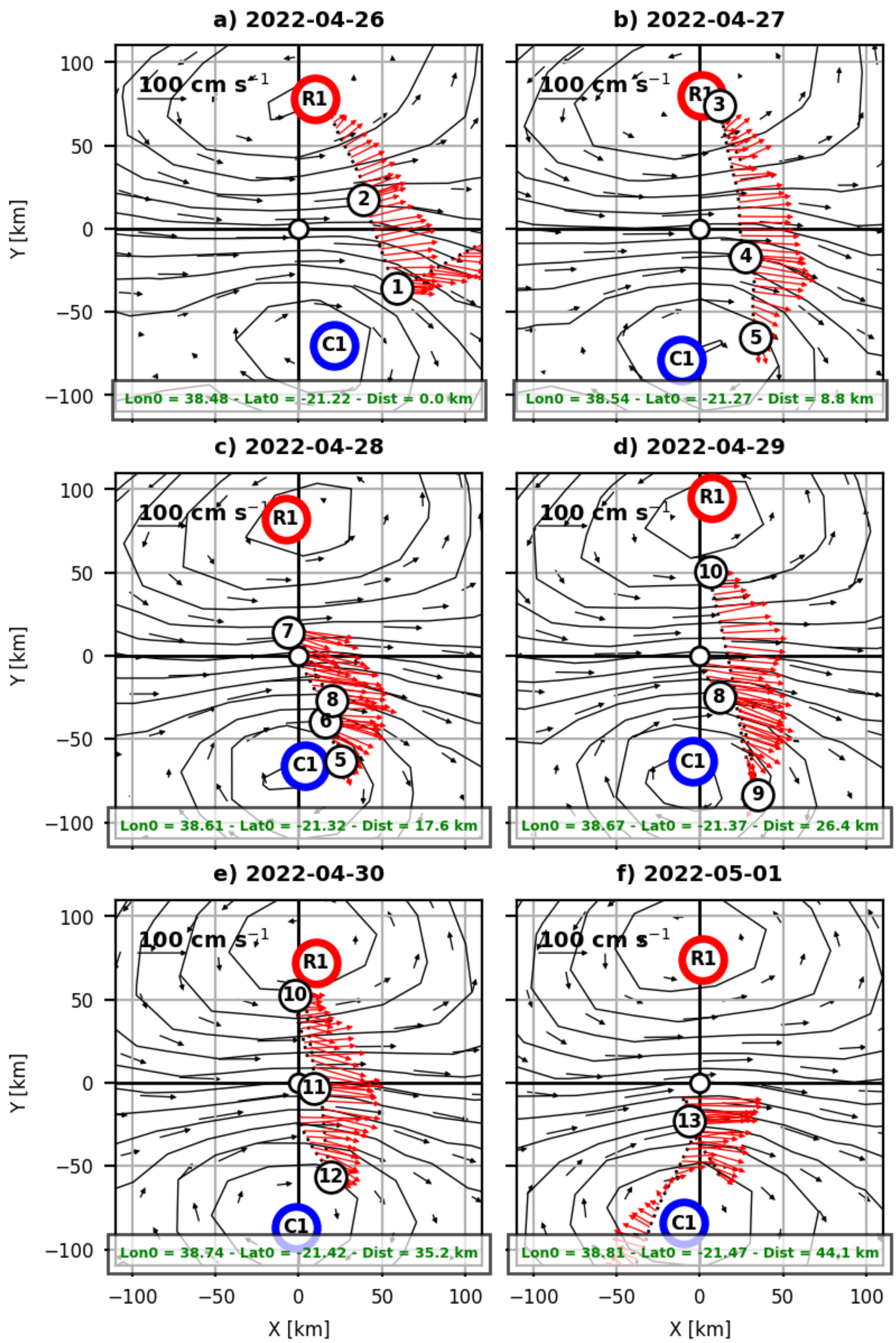

Figure 5. Daily subsurface velocities in the dipole frame for each cruise day. Stations positions (numbers), SADCP 48 m velocities (depth chosen below the Ekman depth - red arrows), altimetry SSH (1 black contour / 5 cm) and altimetry derived geostrophic (black arrows) currents in a regular frame relative to the dipole position (Lon0, Lat0 and distance traveled is provided at the bottom of each panel) and orientation (Θ=115°) for each day. The dipole is relatively stable in the frame.

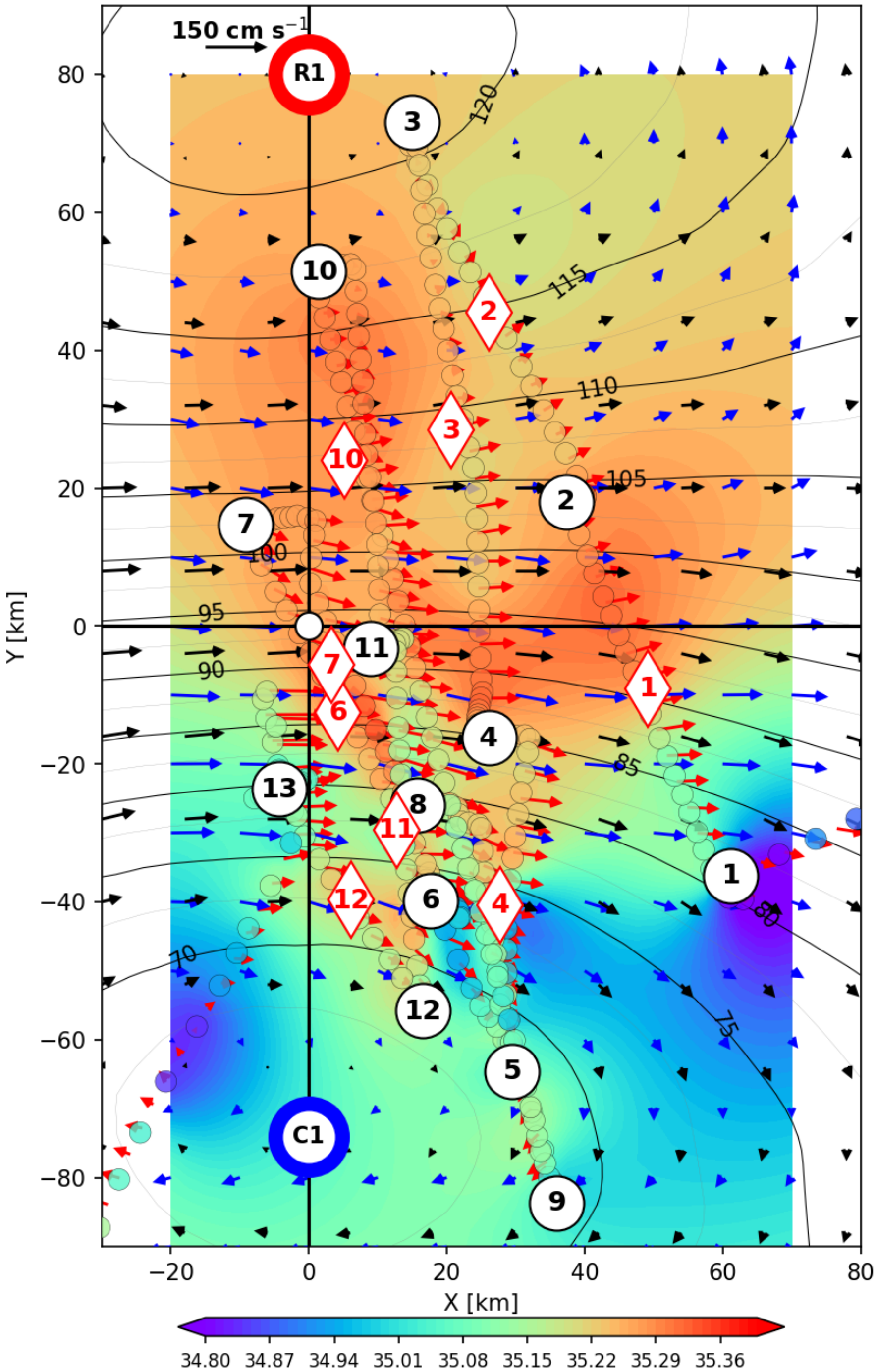

Figure 6. Velocities and tracers mapping on a regular grid. Altimetry SSH (black contours - 1 contour / 5 cm) and altimetry derived geostrophic velocities (black arrows) averaged over the duration of Leg 1 (from April 19 to May 24, 2024) , TSG sea surface salinity [PSS.78] (colors) and SADCP 48 m velocities (red arrows: along the cruise tracks, blue arrows: after mapping) for the cruise. Stations are presented as black numbers into circles and central locations of MVP vertical sections as red numbers into diamonds. MVP operations were not conducted on sections 5, 8, and 9. Note the homogeneous SSS between 35.2 and 35.3 g kg^{-1} in R1 (Y>0) and the variability ranging from 34.8 to 35.3 g kg^{-1} in C1 (Y<0).

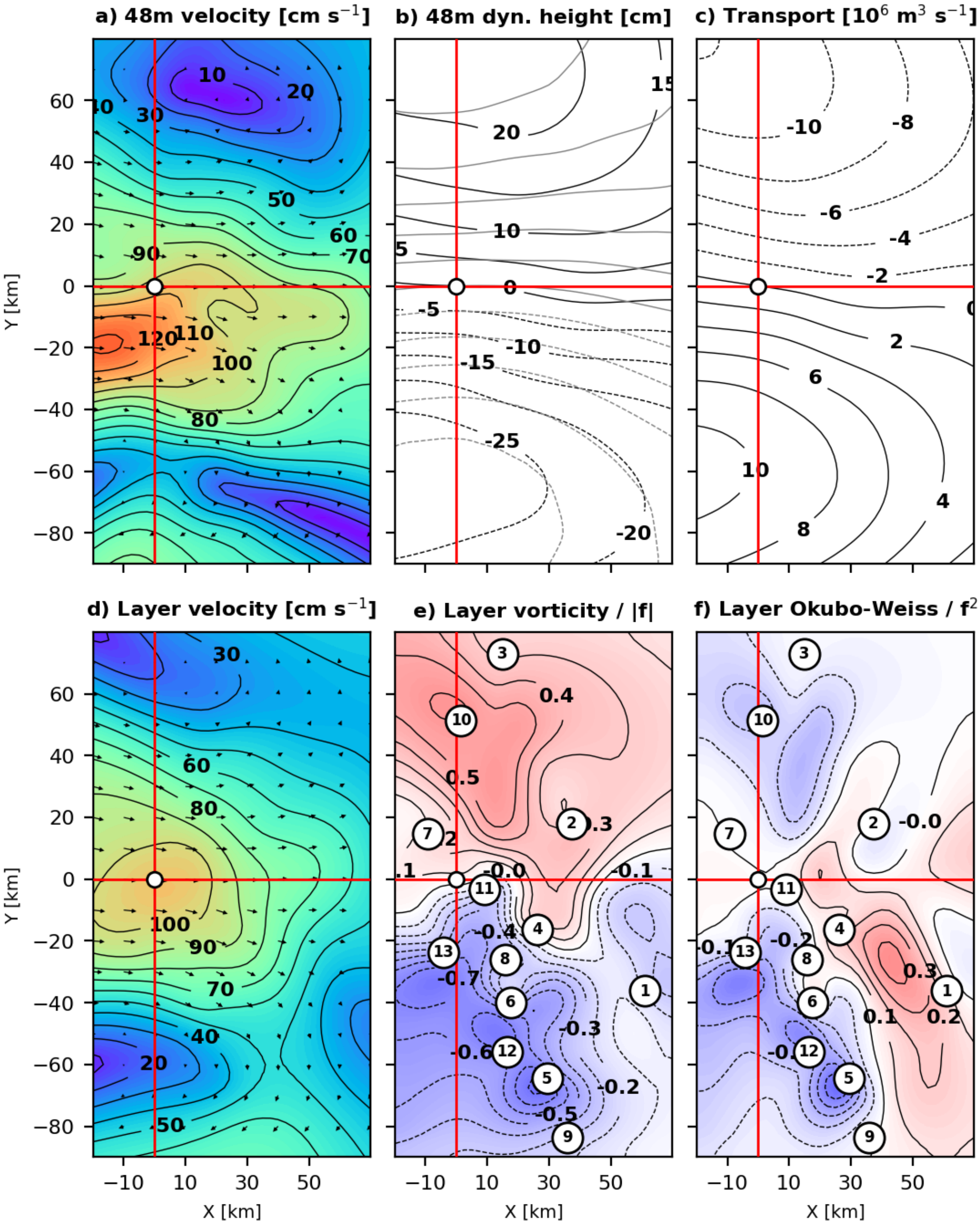

Figure 7. Mean mesoscale transport and dynamical structure for the upper ocean. a) Gridded SADCP velocities at 48 m [cm s^{-1}]. b) Dynamic height [cm] from gridded SADCP velocities at 48 m (black contours) compared with altimetry SSH (gray contours). c) Integrated transport [10^6 m^3 s^{-1}]. d) Vertically averaged velocities [cm s^{-1}] over 250 m. e) Vorticity divided by the Coriolis parameter, averaged over 250 m. f) Okubo-Weiss parameter divided by the Coriolis parameter squared, averaged over 250 m. The horizontal axes are in kilometers, centered over the dipolar structure. The stations are presented as numbers in circles. Note the clear separation between R1 and C1 and the meander in the front.

center, vertically averaged velocities still exceed 110 cm s^{-1}. From this, we derived a transport function for the first 250 m, showing that at least 10 Sverdrups (1 Sv = 10^6 m^3 s^{-1}) pass through the central part of the dipole (for -20 km < Y < 20 km, Figure 7-c).

Vertically averaged vorticity ($\bar{\xi} = \frac{\partial \bar{v}}{\partial x} - \frac{\partial \bar{u}}{\partial y}$) delineates the anticyclonic ring ($\xi >$ 0 in the Southern Hemisphere) from the cyclonic eddy (Figure 7-e). Typical anticyclonic values of $\bar{\xi}$ / $|f|$ are around 0.5. Vorticity reaches its maximum at 100 m, with values exceeding 0.9, approaching the threshold for inertial instability (not shown). Absolute values in Figure 7-e are larger for the cyclone than for the anticyclone, as the eddy is smaller. A meander appears to develop in the central part of the dipole (Y = 0; 0 < X < 50 km) with a wavelength of approximately 40 km.

The vertically averaged Okubo-Weiss parameter ($\bar{W} = (\frac{\partial \bar{u}}{\partial x} - \frac{\partial \bar{v}}{\partial y})^2 + (\frac{\partial \bar{v}}{\partial x} + \frac{\partial \bar{u}}{\partial y})^2 - \xi^2$) distinguishes the elliptic regions dominated by rotation, such as rings or eddies (for $\bar{W} < 0$), from the hyperbolic regions dominated by deformation, such as fronts (for $\bar{W} >$ 0) (Figure 7-f). Like vorticity, the Okubo-Weiss parameter clearly defines the central axis of the dipole (Y = 0), with station 11 close to the dipole center. It separates clearly the hyperbolic difluent side of the dipole where $\bar{W} > 0$.

By utilizing both vorticity and the Okubo-Weiss parameter, we can unambiguously classify the stations based on their locations within the anticyclonic ring, the cyclonic eddy, or the frontal region in between. This type of classification has been previously used for biological applications in the Mozambique Channel (for example, from altimetry SSH) (Lamont et al., 2014). Here, we obtained the following classification which could be used for further biogeochemical, biological and ecological studies:

Anticyclonic Ring: Stations 3, 7, and 10 (with station 7 being close to the central front).

Cyclonic Eddy: Stations 5, 6, 8, 12, and 13 (with stations 8 and 13 being close to the central front).

Dipole Center: Station 11 almost exactly at the dipole center.

Edge of Cyclone and Meander: Station 4 on the edge of the cyclone, close to a small meander in the front.

Outer Edge of Anticyclonic Ring: Station 2 on the outer edge of R1.

Outer Edge of Cyclonic Eddy: Station 9, south of the dipolar influence.

Dipole Periphery: Station 1, the first station made at the beginning of Leg 1, before arriving in the dipole, under the influence of the dipole, but on the outer edge of C1.

3.4 Vertical structure of the dipole

Figure 8 presents cross-sections of conservative temperature [°C] (left) and practical salinity [g kg^{-1}] (right) obtained from the MVP, represented in the dipole frame. Typical of the Mozambique Channel for this season, the temperature in the mixed layer was quite homogeneous around 28°C. Sea surface temperature (SST) can not clearly separate the structures. Inside the dipole, isotherms exhibited large-scale doming associated with the cyclonic eddy for Y < 0 (sections 1, 4, 6, 11) and were relatively flat in the anticyclone (Y > 0, sections 2, 3, 10). These temperature values align with expectations from the World Ocean Atlas 2023 (Reagan et al., 2024).

Salinities in C1 exhibit notable variations, with minimum values (< 35.2 g kg^{-1}) observed within the mixed layer (Figure 8; X < 10 km for sections 1, 4, 6, 7, 11, and 12) and higher values (> 35.4 g kg^{-1}) between 50 m and 200 m. Sharp gradients and patchiness are also evident in the mixed layer. The elevated values below this layer are associated with slanted layers extending between C1 and R1 in all sections. A larger patch of higher salinity (> 35.5 g kg^{-1}) can be seen between 100 and 250 m on section 1. Small patches with salinity values also exceeding 35.5 g kg^{-1} are observed near the dipole axis

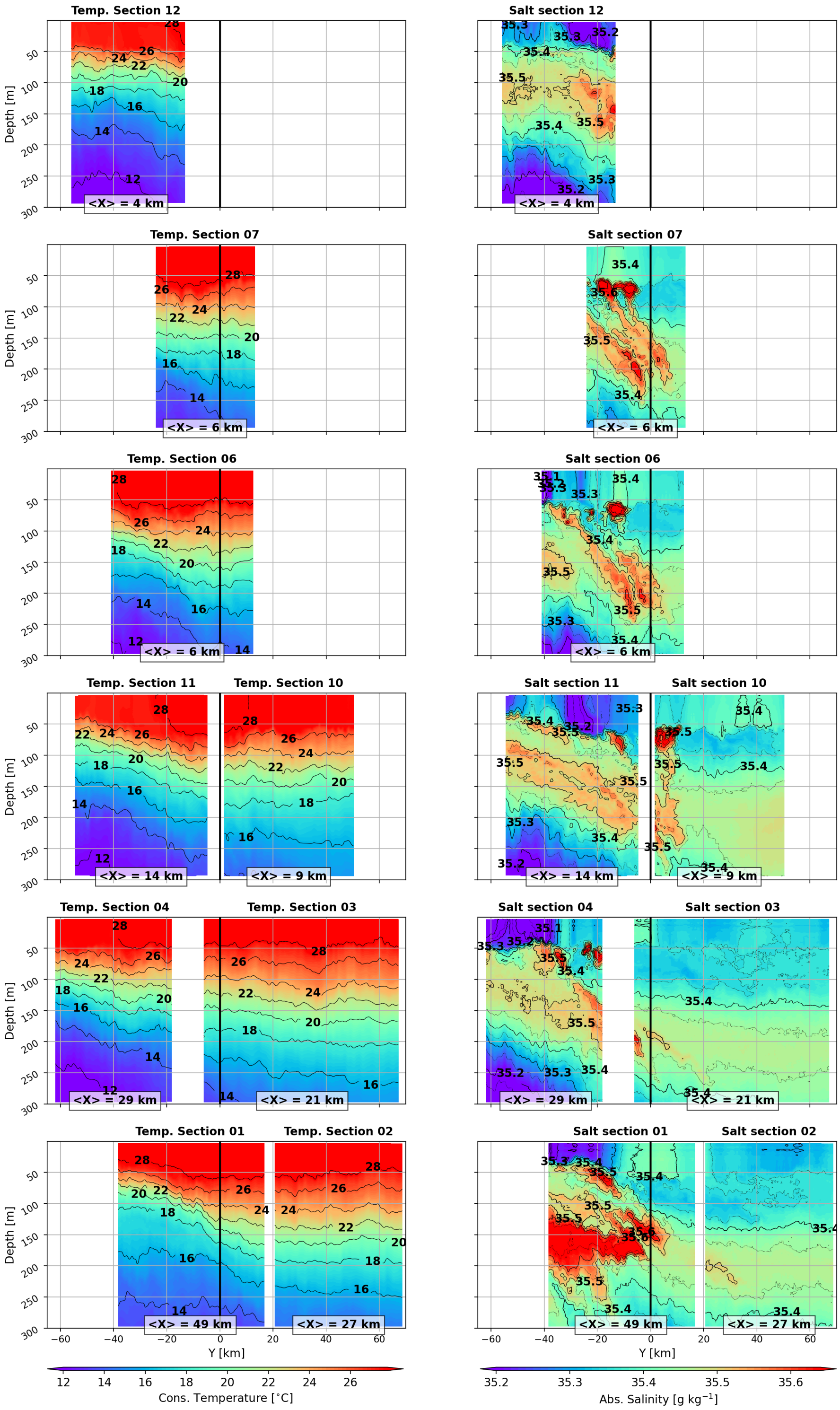

Figure 8. MVP observations in the dipole. Conservative temperature [°C] (left) and practical salinity [g kg^{-1}] (right) MVP cross sections in the dipole frame. Average East-West ⟨ X ⟩ locations are given for each section, from the westernmost (smaller ⟨ X ⟩, top) to the easternmost (larger ⟨ X ⟩, bottom). Sections numbers are defined in Figure (6). Small structures stacked over the vertical are observed in salinity.

just below the mixed layer (just below 50 m), close to the central front (Figure 8; sections 4, 6, 7, 10, 11). Lower salinities, with values below 35.3 g kg^{-1}, show a doming below 200 m in C1 (see sections 11 and 12 in Figure 8). In contrast, isohalines are much flatter in R1 (Figure 8; sections 2, 3, 10). R1 appears to transport Tropical Surface Waters (TSW) with lower salinity (around 35.4 g kg^{-1}) from the north above 150 m, while higher salinities are present between 150 m and 300 m.

This is illustrated by the TS diagrams presented in Figure 9. In panel 9-a, R1 is characterized by relatively homogeneous Tropical Surface Water (TSW, $\sigma_0 > 25.5$ kg m^{-3}) (Beal et al., 2006; Lutjeharms, 2006), with salinities near 35.4 g kg^{-1}. This lies above the Subtropical Surface Water (STSW, $\sigma_0 \sim$ 25.5-26.4 kg m^{-3}) (Beal et al., 2006; Lutjeharms, 2006), exhibiting a diluted salinity maximum of 35.5 g kg^{-1} at $\sigma_0 = 26$ kg m^{-3}. These observations are consistent with the World Ocean Atlas 2023 climatology (Reagan et al., 2024).

In panel 9-b, C1 displays a more complex structure. At the surface (above $\sigma_0 =$ 23.5 kg m^{-3}), C1 is characterized by warm, low-salinity TSW, potentially also influenced by river discharge. Just beneath, a salinity maximum near 35.8 g kg^{-1} suggests the presence of Arabian Sea High Salinity Water (ASHSW) (Kumar & Prasad, 1999) around σ_0 = 23 kg m^{-3}, corresponding to the high-salinity patches observed at the front in Figure 8. Below this layer, significant salinity variations, ranging from 35.35 g kg^{-1} to over 35.6 g kg^{-1}, are observed, corresponding to the slanted layers depicted in Figure 8. A second subsurface salinity maximum, nearly 35.7 g kg^{-1} at $\sigma_0 \approx 26$ kg m^{-3}, is indicative of Subtropical Surface Water (STSW). Below $\sigma_0 = 26.4$ kg m^{-3}, the sharp decline in temperature and salinity marks the transition to South Indian Central Water (SICW) (Beal et al., 2006). The spiraling of contrasted water masses within C1 creates multiple temperature-salinity combinations along isopycnals, contributing to the wide variability observed in the profiles in Figure 9-b.

Observed currents highlight significant differences between R1 and C1 (not shown). Within the ring and the central jet, large currents can reach velocities of up to 150 cm s^{-1}. In contrast, C1 is shallower, with weaker velocities below 150 m, underlying its baroclinic nature. R1, on the other hand, extends to greater depths, a characteristic typical of Mozambique Channel anticyclonic rings (de Ruijter et al., 2002).

4 Vertical velocities in the dipole

Using the gridded tracers and velocities defined in sections 3.3 and 3.4, we derived vertical velocities w from the QG Omega equation. Figure 10 presents an example of temperature, horizontal and vertical velocities at 104 m depth (i.e. below the mixed layer and/or the euphotic zone).

The warm anticyclone and colder cyclone create a temperature front between them, with a relatively smaller meander (as seen from vorticity in section 3.3.2) around Y $\sim$ -20 km. This meander, with along-front and cross-frontal length scales of approximately 30 km, aligns with the maximum velocities in the central jet, which exceed 120 cm s^{-1} at 104 m depth.

Vertical velocities exhibit a complex pattern at different scales, dominated by this meander and consistent with the temperature patterns. Downwelling reaches 30 m day^{-1} around X = 0, Y $\sim$ -10 km, transporting warm surface waters to greater depths. This process promotes vertical mixing and may facilitate the subduction of surface waters into deeper layers. Upwelling reaches nearly 40 m day^{-1} around X = 35 km, Y = -25 km, bringing colder water from below.

Beyond the pattern associated with the meander, weaker vertical velocities related to the larger-scale dipolar structure are observed. Upwelling (with values $\sim$ 10 m day^{-1})

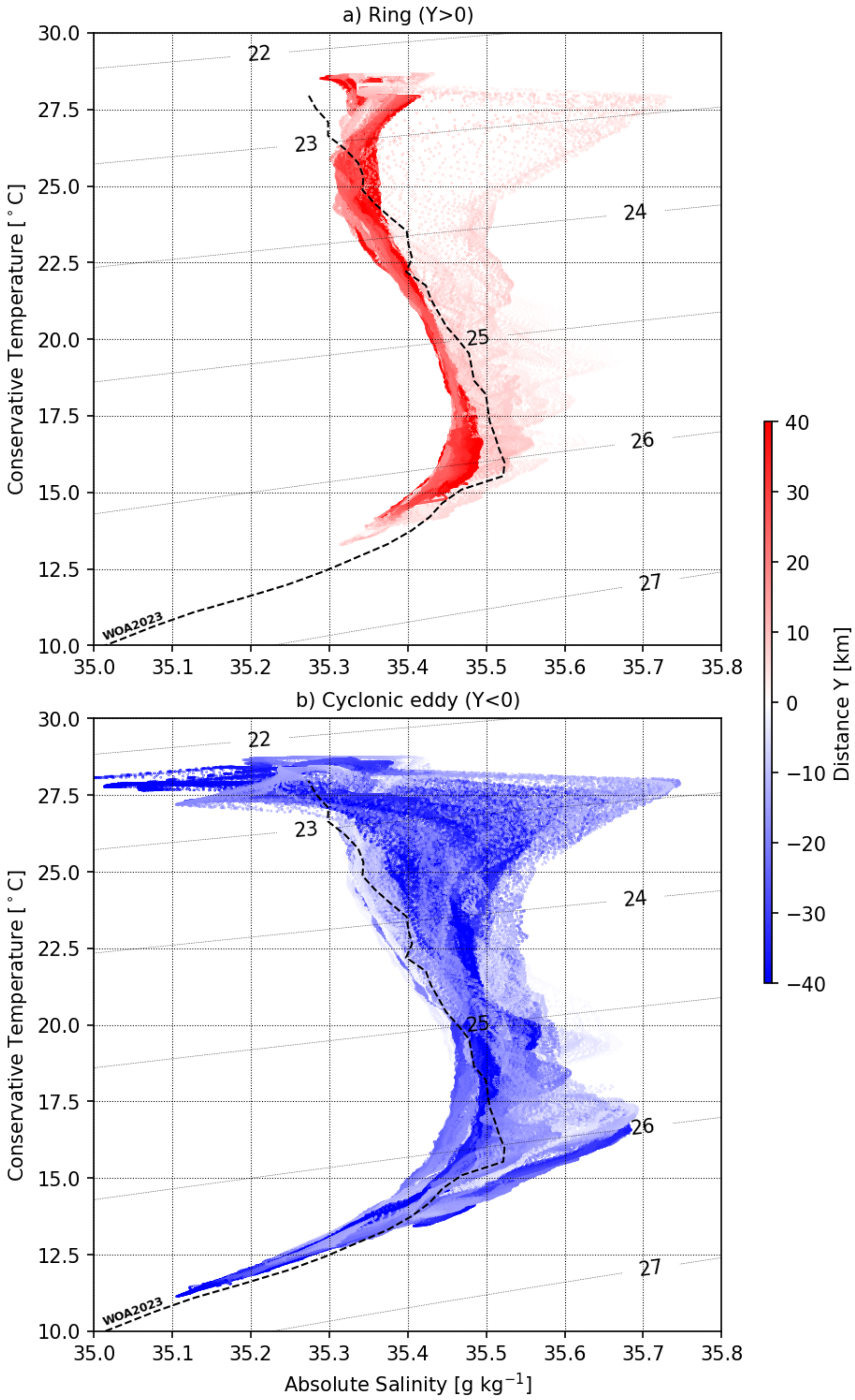

Figure 9. TS diagram as a function of the locations in R1 (top) and C1 (bottom). Conservative temperature [°C] / absolute salinity [g kg^{-1}] diagram for all MVP observations. Dotted contours represent potential density anomalies σ_0 [kg m^{-3}]. Colors represent the cross front distance [Y, km] in the dipole frame (positive toward R1, negative toward C1). The black dotted line is indicative of the World Ocean Atlas 2023 climatology for the month of April for this location. Note the contrasts in water properties between R1 (a; orange-red) and C1 (b; blue-green).

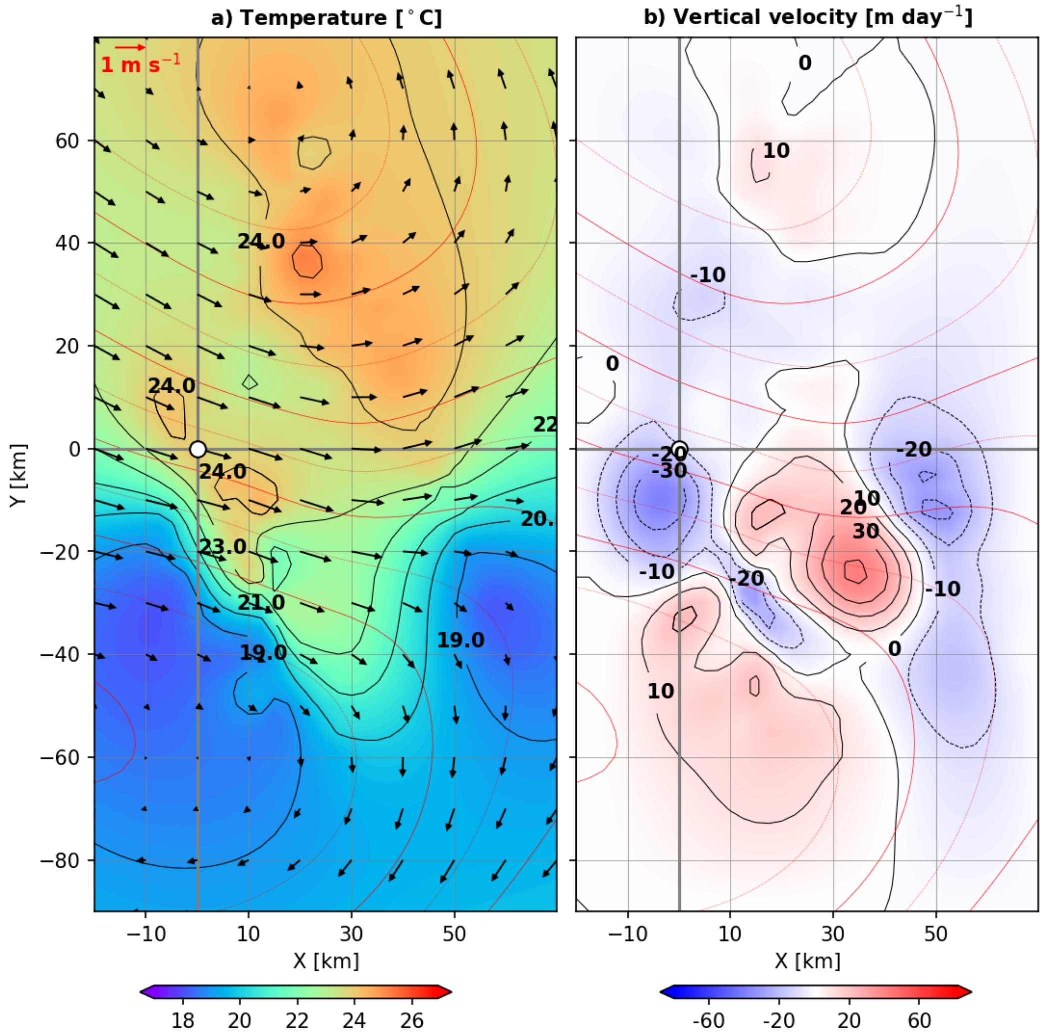

Figure 10. Vertical velocities from the Omega equation at 104 m. Temperature [$^\circ$C] and horizontal velocity (a) and vertical velocity [m day^{-1}] (b) for 104 m depth. Dynamic height derived from gridded velocities (1 red contour / 5 cm) is given on each panel as a streamfunction. The vertical velocity pattern appears associated with the meander in the front.

occurs in the X > 0 sector (corresponding to the difluent sector) of the cyclonic eddy. Conversely, weak downwelling appears dominant in the difluent sector of R1 (X > 0; Y > 0).

Overall, the small meander dominates the vertical velocity field, reaching $\sim$ 40 m day^{-1}, while the larger-scale pattern associated with the dipole exhibits velocities around $\sim$ 10 m day^{-1}, mostly positive in the difluent region of C1 (X > 0; Y < 0) and negative in the difluent region of R1 (X > 0; Y > 0), consistent with previous studies on dipoles (Ni et al., 2020).

5 Origin of water in the dipole

Figure (11) illustrates the backward trajectories of Lagrangian particles released uniformly across three distinct regions on April 29, 2022: R1 (Figure 11-a; 16411 particles), the central jet (Figure 11-b; 1681 particles), and C1 (Figure 11-c; 8156 particles). These particles were advected backward using geostrophic velocities derived from altimetry. For R1 and C1, particles were seeded within the loops defined by the largest closed SSH contour encompassing the corresponding SSH extrema. In the central jet, particles were seeded in the central region where geostrophic velocities exceeded 1 m s^{-1}.

In R1, particles exhibited homogeneous trapping and behavior, slowly moving southward and then southeastward over an extended period. In contrast, the jet displayed very rapid movement from the shelf, with particles traveling from the shelf edge to the central dipole in less than a week, originating from both the south and the north along Sofala Bank. C1 presented a more complex pattern, with a mix of particles originating from the south and moving with C1 since its generation, as well as particles from Sofala Bank, sometimes near the Zambezi river mouth, becoming trapped in the structure as an earlier filament during dipole formation. This intricate behavior reflects the interactions and varying origins of water masses within the cyclone.

Figure 12 presents the time it took for a particle to travel from the shelf (h < 500 m) to its position on April 29, 2022, using 60,000 particles. The results show significant differences between the regions within the dipole. In R1, particles exhibit long travel times, often exceeding 100 days, indicating a long isolation from the coast. Conversely, the central jet demonstrates very rapid transit, with particles taking less than a week to reach their positions, highlighting the jet's efficiency in transporting material from the shelf. C1 reveals a clear spiral structure in the travel times, with alternating low and high values encircling each other, showing contrasting origins of water masses.

6 Summary, discussion and conclusion

During the first leg of the RESILIENCE cruise, we clearly identified a mesoscale eddy-ring dipole in the central Mozambique Channel. This feature consisted of a large anticyclonic ring coupled with a smaller cyclonic eddy on its southern flank, forming in April 2022 and propagating southeastward across the channel. For the first time, high-resolution, in-situ measurements provided insights into the dynamics of a Mozambique eddy-ring dipole, revealing characteristics such as a strong central jet, significant vertical velocities driven by smaller structures, patchiness and layering on the cyclonic side, and the contrasted influence of coastal waters on the dipole's structure.

Large offshore transport

The velocity structure of the dipole revealed a narrow central jet with horizontal surface velocities reaching up to 130 cm s^{-1}, and vertically averaged velocities over 250 meters exceeding 110 cm s^{-1}. Such high velocities were already previously observed in a similar dipole at almost the same location in 2007 (Ternon, Roberts, et al., 2014). This suggests that these structures could be relatively recurrent in the central Mozambique

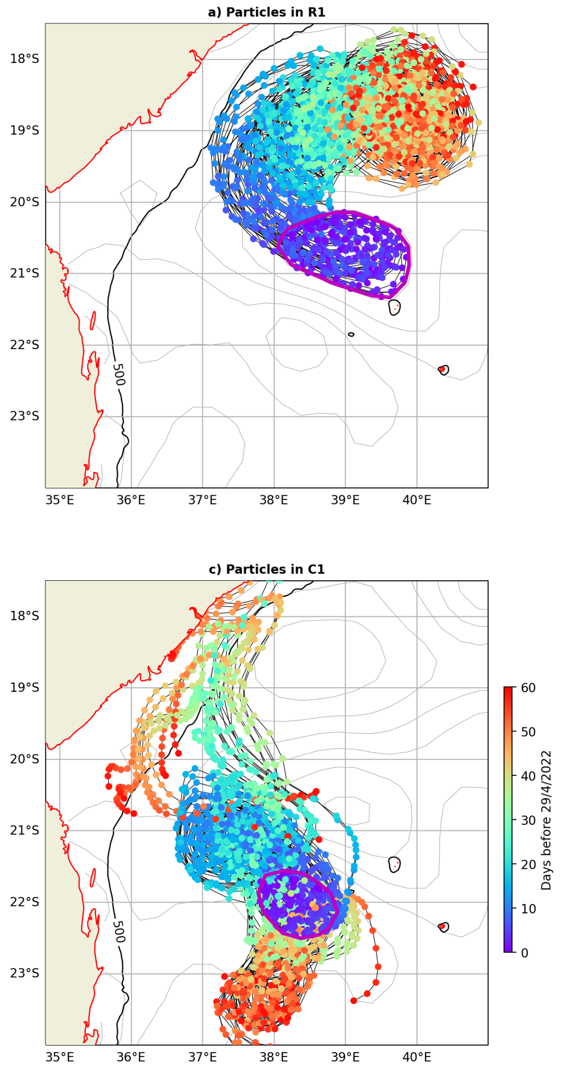

Figure 11. Origin of water in the structures. Backward trajectories and number of days (colors) before the release for particles released uniformly on April 29, 2022 in R1 (a; 16411 particles), in the central jet (b; 1681 particles) and in C1 (c; 8156 particles). Each panel displays only a subset of 40 particles. Each dot represents a day. R1 shows a strong coherence over a long time periode, while C1 presents multiple water origins. The central jet is associated with fast movements from the shelf.

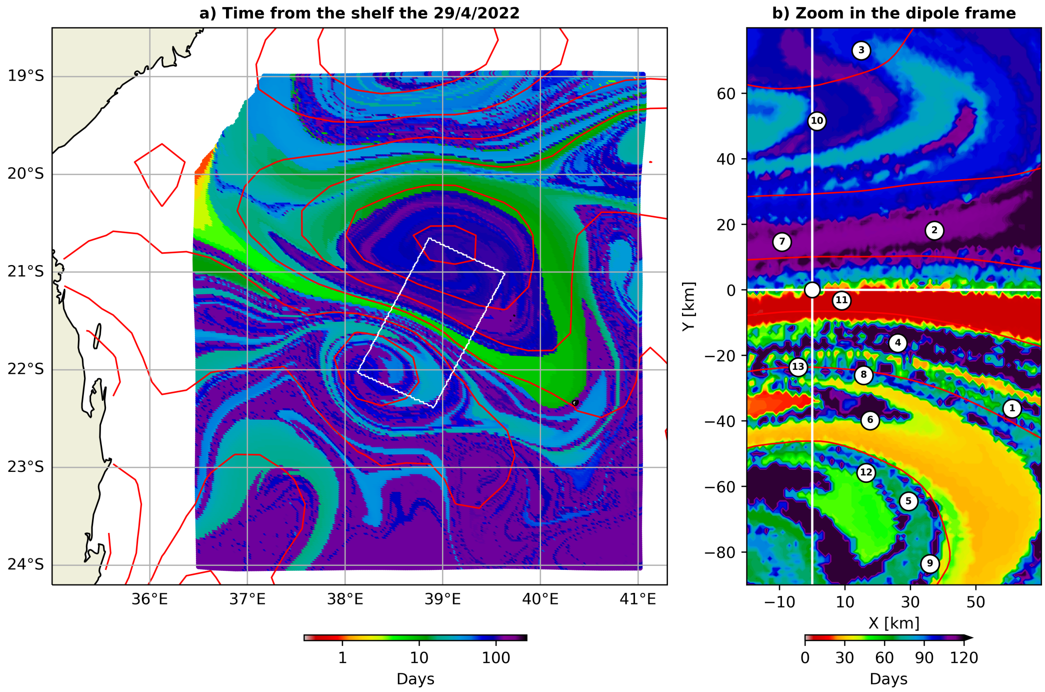

Figure 12. Connectivity with the shelves. a) Time [days] for a particle to go from the shelf to it's location the 29$^{\text{th}}$ of April 2022. b) Zoom in the dipole frame (seen as a white box on panel a) with the stations positions. Although R1 is relatively isolated from the coast, the connection between the shelf and the center of the dipole is achieved here in less than a week. Sharp gradients are visible in C1.

Channel. This strong jet allowed a significant mean transport of over 10 Sverdrups through the dipole, highlighting its role in the eastward "vacuum" of water from the Mozambican coast, consistent with previous studies (Roberts et al., 2014). Huang et al. (2024) reported an average of nearly three dipoles per year occurring in the central Mozambique Channel, around 18°S. Based on their Figure 8, we could infer a mean lifespan of approximately 20 days for these dipoles, which aligns with the 24-day lifespan observed in our current study. This suggests that the central Mozambique Channel could be influenced by dipole eddies for roughly two months each year. Given the substantial transports observed, these dipole eddies likely play a significant role in cross-shore transport, supporting the important eddy offshore transport highlighted in model simulations by José et al. (2016).

However, the magnitude of this transport depends on the integration depth and could be larger if extended beyond 250 meters. The transport direction also varies based on the eddy configuration, with the cyclonic eddy on the southern flank ensuring eastward, offshore transport (Roberts et al., 2014). Further analysis of these dipole structures is needed to generalize the current findings. If cyclonic eddies were primarily generated by vortex stretching due to interactions of anticyclonic eddies with the shelf edge (Sutyrin & Grimshaw, 2010), this should favor (for a ring propagating southward along a western boundary) the formation of dipoles with cyclonic eddies to the south of the ring.

Vertical velocities dominated by smaller scale structures

The stability of the mesoscale dipole during the observation period allowed us to map the variables over a moving frame and derive vertical velocities using the QG Omega equation. These vertical velocities, reaching 40 m day^{-1} at 104 m depth, were not dominated by the dipole itself but by a smaller-scale meander in the central jet. These smaller scale upwelling and downwelling patterns aligned with temperature signals, with warmer water associated with downwelling and colder water with upwelling. Such smaller-scale dominance in vertical velocities and, consequently, nutrient fluxes, should be expected as vertical fluxes increase with model resolution (Lévy et al., 2001).

Nevertheless, the larger scale influence of the mesoscale dipole remained apparent, characterized by dominance of weaker positive vertical velocities in the cyclonic difluent region and dominance of negative values in the anticyclonic difluent region. This pattern aligns with the general structure outlined by Ni et al. (2020), though it represents only a partial view of the quadripolar configuration they described. Note that the correlation between cyclonic (anticyclonic) vorticity and upwelling (downwelling) is here only a result of the incomplete capture of the dipole's full structure.

Several potential sources of error, such as synopticity loss, gridding parameters sensitivity or boundary conditions influence (Buongiorno Nardelli, 2013; Pidcock et al., 2013) were considered, but the stability of the structure and careful selection of boundary conditions minimized these concerns. Nevertheless, the sensitivity of the absolute values to the decorrelation scales used in the objective analysis necessitates cautious interpretation of the vertical velocity estimates. The limitation of observations to the upper 250 meters offers only a partial view, as the Mozambique Channel anticyclonic ring may probably extend deeper (de Ruijter et al., 2002). Future research should focus on estimating vertical nutrient fluxes based on these vertical velocities, which will also require high-resolution nutrient observations.

Patchiness and coastal influence

One of the most striking observations during the RESILIENCE cruise was the pronounced layering and patchiness in salinity within C1 and the front. This appeared as large excursions along isopycnals in the TS diagram for the cyclonic eddy. Lagrangian backtracking suggests that this patchiness could be linked to the spiraling structure within the cyclonic eddy, possibly due to an earlier filament of water being trapped during dipole formation. This earlier filament around R1 can be seen on satellite imagery (see Figure 2-f). This spiraling of water with different origins contrasts with the relatively homogeneous Mozambique Channel anticyclonic ring R1 and highlights the importance of stirring in shaping the properties of the dipole front and C1. This observed patchiness could have significant implications for biological distributions, with the intricate layering within the cyclonic eddy underscoring the complex interactions of stirring and mixing processes at play.

Conclusion

The Mozambique Eddy-Ring Dipoles are prominent features in the central Mozambique Channel. Through an innovative adaptive sampling strategy that tracks their movement, we have shown that these structures are characterized by strong currents that induce significant stirring, leading to the formation of filaments and contrasting water masses spiraling around the cyclonic core. Our results emphasize the role these dipoles play in the rapid and efficient transport of properties from the continental shelf to the open ocean, and their potential importance in the connectivity between ecosystems in the region. While vertical velocities may play a secondary role at mesoscale, the influence of sub-mesoscale processes, such as small meanders, layering, and instabilities, warrants further investigation to fully comprehend the dynamics involved. This study moves beyond the traditional cyclone/anticyclone/front paradigm, offering new insights into the complex dynamics that govern the formation, evolution, and internal structure of eddy-ring dipoles in the Mozambique Channel. These findings align with biogeochemical and ecological observations at similar scales during RESILIENCE, particularly in relation to phytoplankton, trace metals, and CO2 (Ternon et al., 2023). The insights gained from this work provide a valuable foundation for future studies investigating the influence of Mozambique Channel dipoles on biogeochemical, biological and ecological processes in the region.

Open Research Section

Satellite observations presented here are distributed by Copernicus Marine Services for surface chlorophyll (Colella et al., 2024) and for absolute dynamic topography (Pujol, 2024).

Post processed MVP temperature and salinity measurements are available on SEANOE (L'Hégaret et al., 2024).

In-situ observations collected during the RESILIENCE cruise will be integrated for distribution in the SISMER (Ternon et al., 2022, 2023).

Acknowledgments

The RESILIENCE oceanographic campaign has been supported by the French National Oceanographic Fleet, by the Belmont Forum Ocean Front Change project, implemented through the French National Research Agency (ANR-20-BFOC-0006-04), by the ISblue project, Interdisciplinary graduate school for the blue planet (ANR-17-EURE-0015) and co-funded by a grant from the French government under the program "Investissements d'Avenir" embedded in France 2030, and by the French National program LEFE (Les Enveloppes Fluides et l'Environnement). We extend our gratitude to the technical team responsible for the observations, instruments deployment and data calibration for RESILIENCE, including Denis Diveres, Jean-Luc Fuda, Caroline Le Bihan, Philippe Le Bot, Olivier Ménage, and Loic Quemener. GENAVIR (France) provided the technical support for the deployment of the MVP (Moving Vessel Profiler) which was critical for the success of this campaign. We also thank the crew of the R/V Marion Dufresne for their invaluable assistance, as well as the Master's students from the Floating University (Université de Bretagne Occidentale, Université du Littoral Côte d'Opale, Université Côte d'Azur) and their coordinators. We acknowledge the use of OpenAI's ChatGPT-4 for assistance in refining and correcting language, and enhancing the clarity of this manuscript The cruise's adaptive tracking and sampling were informed by real-time observations from the Ocean Virtual Laboratory (https://ovl.oceandatalab.com/; funded by the European Space Agency) and from the Copernicus Marine Service.

References

Arhan, M., & De Verdière, A. C. (1985). Dynamics of eddy motions in the eastern North Atlantic. *J. Phys. Oceanogr.*, *15*, 153-170.

Backeberg, B. C., & Reason, C. J. C. (2010). A connection between the South Equatorial Current north of Madagascar and Mozambique Channel eddies. *Geophys. Res. Lett.*, *37*, L04604.

Barlow, R., Lamont, T., Morris, T., Sessions, H., & van den Berg, M. (2014). Adaptation of phytoplankton communities to mesoscale eddies in the Mozambique Channel. *Deep Sea Res., Part II*, *100*, 106-118.

Beal, L. M., Chereskin, T. K., Lenn, Y. D., & Elipot, S. (2006). The sources and mixing characteristics of the Agulhas current. *J. Phys. Oceanogr.*, *36*, 2060-2074.

Buongiorno Nardelli, B. (2013). Vortex waves and vertical motion in a mesoscale cyclonic eddy. *J. Geophys. Res.*, *118*, 5609–5624.

Chelton, D. B., deSzoeke, R. A., Schlax, M. G., Naggar, K. E., & Siwertz, N. (1998). Geographical variability of the first-baroclinic Rossby radius of deformation. *J. Phys. Oceanogr.*, *28*, 433-460.

Colella, S., Böhm, E., Cesarini, C., Jutard, Q., & Brando, V. (2024). *Global Ocean Colour (Copernicus-GlobColour), Bio-Geo-Chemical, L3 (daily) from satellite observations (near real time).* E.U. Copernicus Marine Service Information (CMEMS). Marine Data Store (MDS). doi: 10.48670/moi-00278

Cossa, O., Pous, S., Penven, P., Capet, X., & Reason, C. J. C. (2016). Modelled cyclonic eddies in the Delagoa Bight region. *Cont. Shelf Res.*, *19*, 14-29.

de Ruijter, W. P. M., Ridderinkhof, H., Lutjeharms, J. R. E., Schouten, M. W., & Veth, C. (2002). Observations of the flow in the Mozambique Channel. *Geophys. Res. Lett.*, *29*, 1401-1403.

Ganachaud, A., & Wunsch, C. (2000). Improved estimates of global ocean circulation, heat transport and mixing from hydrographic data. *Nature*, *408*, 453-457.

Halo, I., Backeberg, B., Penven, P., Ansorge, I., Reason, C., & Ullgren, J. (2014). Eddy properties in the Mozambique Channel: A comparison between observations and two numerical ocean circulation models. *Deep Sea Res., Part II*, *100*, 38-53.

Harlander, U., Ridderinkhof, H., Schouten, M. W., & de Ruijter, W. P. M. (2009). Long-term observations of transport, eddies, and Rossby waves in the Mozambique channel. *Geophys. Res. Lett.*, *114*, C02003.

Hoskins, B. J., Draghici, I., & Davies, H. C. (1978). A new-look at the ω-equation. *Quart. J. Roy. Meteor. Soc.*, *104*, 31-38.

Huang, T., Zhou, F., Ma, X., Zeng, D., Tang, Y., Ma, Y., . . . Huang, D. (2024). Characteristics and generation mechanisms of anticyclonic eddies, cyclonic eddies and dipole eddies in the Mozambique Channel. *Front. Mar. Sci.*, *11*, 1375367.

Jaquemet, S., Ternon, J., Kaehler, S., Thiebot, J., Dyer, B., Bemanaja, E., . . . Le Corre, M. (2014). Contrasted structuring effects of mesoscale features on the seabird community in the Mozambique Channel. *Deep Sea Res., Part II*, *100*, 200-211.

José, Y. S., Aumont, O., Machu, E., Penven, P., Moloney, C. L., & Maury, O.

(2014). Influence of mesoscale eddies on biological production in the Mozambique Channel: Several contrasted examples from a coupled ocean- biogeochemistry model. *Deep Sea Res., Part II*, *100*, 79-93.

José, Y. S., Penven, P., Aumont, O., Machu, E., Moloney, C. L., Shillington, F., & Maury, O. (2016). Suppressing and enhancing effects of mesoscale dynamics on biological production in the Mozambique Channel. *J. Mar. Sys.*, *158*, 129-139.

Kermabon, C., Lherminier, P., Le Bot, P., & Gaillard, F. (2018). *CASCADE V7.2: Logiciel de validation et de visualisation des mesures ADCP de coque. documentation utilisateur et maintenance* (Tech. Rep.). LOPS-IFREMER.

Kumar, S. P., & Prasad, T. G. (1999). Formation and spreading of Arabian Sea high-salinity water mass. *J. Geophys. Res.*, *104*, 1455–1464.

Lamont, T., Barlow, R. G., Morris, T., & van den Berg, M. A. (2014). Characterisation of mesoscale features and phytoplankton variability in the Mozambique Channel. *Deep Sea Res., Part II*, *100*, 94-105.

Lamont, T., Roberts, M. J., Barlow, R. G., Morris, T., & van den Berg, M. A. (2010). Circulation patterns in the Delagoa Bight, Mozambique, and the influence of deep ocean eddies. *Afr. J. mar. Sci.*, *32*, 553-562.

Le Bihan, C. (2024). *RESILIENCE 2022 CTD-O_2 data report* (Tech. Rep.). LOPS-IFREMER.

Legal, C., Klein, P., Treguier, A.-M., & Paillet, J. (2007). Diagnosis of the vertical motions in a mesoscale stirring region. *J. Phys. Oceanogr.*, *37*, 1413-1424.

Lévy, M., Klein, P., & Treguier, A.-M. (2001). Impact of sub-mesoscale physics on production and subduction of phytoplankton in an oligotrophic regime. *J. Mar. Res.*, *59*, 535–565.

L'Hégaret, P., Schütte, F., Speich, S., Reverdin, G., Baranowski, D. B., Czeschel, R., … Karstensen, J. (2023). Ocean cross-validated observations from R/Vs *L'Atalante*, *Maria S. Merian*, and *Meteor* and related platforms as part of the EUREC^{4}A-OA/ATOMIC campaign. *Earth System Science Data*, *15*(4), 1801–1830. doi: 10.5194/essd-15-1801-2023

L'Hégaret, P., Ternon, J.-F., Noyon, M., Penven, P., & Herbette, S. (2024). *MVP corrected measurements from RESILIENCE* (Tech. Rep.). SEANOE. doi: 10.17882/99128

Lutjeharms, J. R. E. (2006). *The Agulhas Current*. Springer-Verlag.

Malauene, B. S., Lett, C., Marsac, F., Penven, P., Abdula, S., Moloney, C. L., & Roberts, M. J. (2024). Influence of Mozambique Channel eddies on larval loss of two shallow-water commercial shrimp species. *PLOS Clim.*, *3*, e0000414.

Malauene, B. S., Moloney, C. L., Lett, C., Roberts, M. J., Marsac, F., & Penven, P. (2018). Impact of offshore eddies on shelf circulation and river plumes of the Sofala Bank, Mozambique Channel. *J. Mar. Sys.*, *185*, 1-12.

Malauene, B. S., Shillington, F. A., Roberts, M. J., & Moloney, C. L. (2014). Cool, elevated chlorophyll-a waters off northern Mozambique. *Deep Sea Res., Part II*, *100*, 68-78.

McGillicuddy, D. J., & Robinson, A. R. (1997). Eddy-induced nutrient supply and new production in the Sargasso sea. *Deep Sea Res., Part I*, *44*, 1427-1450.

Ni, Q., Zhai, X., Wang, G., & Hughes, C. W. (2020). Widespread mesoscale dipoles in the global ocean. *J. Geophys. Res.*, *125*, e2020JC016479.

Oschlies, A., & Garçon, V. (1998). Eddy-induced enhancement of primary production in a model of the North Atlantic Ocean. *Nature*, *394*, 266-269.

Penven, P., Halo, I., Pous, S., & Marie, L. (2014). Cyclogeostrophic balance in the Mozambique Channel. *J. Geophys. Res.*, *119*, 1054-1067.

Pidcock, R., Martin, A., Allen, J., Painter, S. C., & Smeed, D. (2013). The spatial variability of vertical velocity in an Iceland basin eddy dipole. *Deep Sea Res., Part I*, *72*, 121-140.

Pinot, J.-M., Tintoré, J., & Wang, D.-P. (1996). A study of the omega equation for diagnosing vertical motions at ocean fronts. *J. Mar. Res.*, *54*, 239-259.

Pivan, X., Krug, M., & Herbette, S. (2015). Observations of the vertical and temporal evolution of a Natal Pulse along the Eastern Agulhas Bank. *J. Geophys. Res.*, *121*, 10.1002/2015JC011582.

Pollard, R. T., & Regier, L. (1992). Vorticity and vertical circulation at an ocean front. *J. Phys. Oceanogr.*, *22*, 609-625.

Pujol, M.-I. (2024). *Global ocean gridded L4 sea surface heights and derived variables nrt.* E.U. Copernicus Marine Service Information (CMEMS). Marine Data Store (MDS). doi: 10.48670/moi-00149

Reagan, J. R., Boyer, T. P., E.García, H., Locarnini, R. A., Baranova, O. K., Bouchard, C., ... Dukhovskoy, D. (2024). *World Ocean Atlas 2023* (Tech. Rep.). NOAA National Centers for Environmental Information.

Roberts, M. J., Ternon, J.-F., & Morris, T. (2014). Interaction of dipole eddies with the western continental slope of the Mozambique Channel. *Deep Sea Res., Part II*, *100*, 54-67.

Rousselet, L., Doglioli, A. M., de Verneil, A., Pietri, A., Della Penna, A., Berline, L., ... Petrenko, A. (2019). Vertical motions and their effects on a biogeochemical tracer in a cyclonic structure finely observed in the Ligurian Sea. *J. Geophys. Res.*, *124*, 3561-3574.

Saëtre, R., & da Silva, A. J. (1984). The circulation of the Mozambique Channel. *Deep Sea Res., Part I*, *31*, 485–508.

Schouten, M. W., de Ruijter, W. P. M., van Leeuwen, P. J., & Ridderinkhof, H. (2003). Eddies and variability in the Mozambique Channel. *Deep Sea Res., Part II*, *50*, 1987-2003.

Sutyrin, G. G., & Grimshaw, R. (2010). The long-time interaction of an eddy with shelf topography. *Ocean Model.*, *32*, 25-35.

Ternon, J. F., Bach, P., Barlow, R., Huggett, J., Jaquemet, S., Marsac, F., ... Roberts, M. J. (2014). The Mozambique Channel: From physics to upper trophic levels. *Deep Sea Res., Part II*, *100*, 1-9.

Ternon, J.-F., Herbette, S., Penven, P., & Noyon, M. (2022). *RESILIENCE cruise, RV Marion Dufresne.* doi: 10.17600/18001917

Ternon, J.-F., Noyon, M., Penven, P., Herbette, S., Artigas, L. F., Toullec, J., ... Chandelier, G. (2023). *RESILIENCE - fRonts, EddieS and marIne LIfe in the wEstern iNdian oCEan, 19 April - 24 May 2022, MD237 R/V Marion Dufresne* (Tech. Rep.). Cruise Report.

Ternon, J. F., Roberts, M. J., Morris, T., Hancke, L., & Backeberg, B. (2014). In situ measured current structures of the eddy field in the Mozambique Channel. *Deep Sea Res., Part II*, *100*, 10-26.

Tew-Kai, E., Rossi, V., Sudre, J., Weimerskirch, H., Lopez, C., Hernandez-Garcia, E., ... Garçon, V. (2009). Top marine predators track Lagrangian coherent structures. *Proc. Natl. Acad. Sci. USA*, *106*, 8245-8250.

Ullgren, J. E., van Aken, H. M., Ridderinkhof, H., & de Ruijter, W. P. M. (2012). The hydrography of the Mozambique Channel from six years of continuous temperature, salinity, and velocity observations. *Deep Sea Res., Part I*, *69*, 36-50.

Weimerskirch, H., Le-Corre, M., Jaquemet, S., Potier, M., & Marsac, F. (2004). Foraging strategy of a top predator in tropical waters: great frigatebirds in the Mozambique Channel. *Mar. Ecol. Prog. Ser.*, *275*, 297-308.